RESEARCH ARTICLE

WILEY

Higher-order-accurate numerical method for temporal stability simulations of Rayleigh-Bénard-Poiseuille flows

Md Kamrul Hasan | Andreas Gross

Department of Mechanical and Aerospace Engineering, New Mexico State University, Las Cruces, New Mexico,

Correspondence

Md Kamrul Hasan, Department of Mechanical and Aerospace Engineering, New Mexico State University, Jett Hall, 1040 South Horseshoe Street, Las Cruces, NM 88003, USA.

Email: kamrul04@nmsu.edu

Summary

For Rayleigh-Bénard-Poiseuille flows, thermal stratification resulting from a wall-normal temperature gradient together with an opposing gravitational field can lead to buoyancy-driven instability. Moreover, for sufficiently large Reynolds numbers, viscosity-driven instability can occur. Two higher-order-accurate methods based on the full and linearized Navier-Stokes equations were developed for investigating the temporal stability of such flows. The new methods employ a spectral discretization in the homogeneous directions. In the wall-normal direction, the convective and viscous terms are discretized with fifth-order-accurate biased and fourth-order-accurate central compact finite differences. A fourth-order-accurate explicit Runge-Kutta method is employed for time integration. To validate the methods, the primary instability was investigated for different combinations of the Reynolds and Rayleigh number. The results from these primary stability investigations are consistent with linear stability theory results from the literature with respect to both the onset of the instability and the dependence of the temporal growth rate on the wave angle. For the cases with buoyancy-driven instability, strong linear growth is observed for a broad range of spanwise wavenumbers. The largest growth rates are obtained for a wave angle of 90°. For the cases with viscosity-driven instability, the linear growth rates are lower and the first mode to experience nonlinear growth is a higher harmonic with half the wavelength of the fundamental.

KEYWORDS

convection, finite differences, linearized Navier-Stokes equations, Rayleigh-Bénard-Poiseuille flow, spectral method, temporal stability code

1 | INTRODUCTION

Plane channel flow between two horizontal parallel plates with temperature gradient in the wall-normal direction and opposing gravitational field is known as Rayleigh-Bénard-Poiseuille (RBP) flow. Plane RBP flows can be found in both nature and engineering designs and have long been investigated by the scientific community. The focus has been particularly on the practical consequences of RBP instability for applications such as solar chimney power plants, ¹ the cooling of electronic components, ^{2,3} chemical vapor deposition reactors, ^{4,5} and many others. Plane RBP flows can exhibit both buoyancy and viscosity-driven instability. ⁶ The onset of flow instability is governed by two dimensionless numbers, the Reynolds number,

Int J Numer Meth Fluids. 2020;1–21. wileyonlinelibrary.com/journal/fld © 2020 John Wiley & Sons, Ltd.

$$Re = \frac{u_{max}h/2}{v},\tag{1}$$

which is here taken with respect to the maximum velocity, u_{max} , channel half-height, h/2, and kinematic viscosity, v, and the Rayleigh number,

$$Ra = \frac{gh^3\gamma\Delta T}{v\alpha^*},\tag{2}$$

with gravitational acceleration, g, volumetric thermal expansion coefficient, γ , temperature difference, ΔT , and thermal diffusivity, α^* .

The hydrodynamic stability of RBP flows has attracted considerable attention in the scientific literature over many years. The influence of thermal stratification on the hydrodynamic stability of incompressible, inviscid, parallel shear flows has been investigated by Miles. Later on, Koppel⁸ derived the linearized disturbance equations for thermally stratified plane parallel flow. Busse and co-authors⁹⁻¹¹ carried out a broad analysis of the stability of horizontally layered flows with vertical temperature gradient. When the convection velocity is zero, hexagonal flow structures can arise above a critical Rayleigh number. 12,13 However, when a streamwise velocity component is added, longitudinal rolls, which are parallel to the flow direction, can appear. The linear temporal stability of RBP flows has first been investigated by Gage and Reid.⁶ The neutral curves for the onset of both buoyancy (critical Rayleigh number, $Ra_c = 1708$) and viscosity-driven (Tollmien-Schlichting [T-S]) instability (critical Reynolds number, $Re_c = 5400$) were established. Orszag¹⁴ found a more accurate value for the critical Reynolds number of $Re_c = 5772.22$. When the Reynolds number is below $Re_c = 5772$ and the Rayleigh number is above $Ra_c = 1708$, buoyancy-driven instability occurs and three-dimensional (3-D) waves with a wave angle of 90° are most amplified. For $Re > Re_c$ and $Ra < Ra_c$, viscosity-driven instability arises and two-dimensional (2-D) T-S waves with a wave angle of zero degree are most amplified. The results of the linear stability theory (LST) analyses for plane RBP flow by Gage and Reid⁶ were confirmed by numerous computational and experimental investigations. Mori and Uchida¹⁵ found longitudinal 3-D flow structures in the experiment that were aligned parallel with the streamwise direction when the temperature difference between the bottom and top wall was increased beyond a threshold value. Nakayama et al¹⁶ established neutral curves based on the wall-normal temperature gradient, ΔT , and a characteristic parameter, μ^* ($\mu^* = Re\tau^*h/\Delta T$, where τ^* is the temperature gradient in the streamwise direction and h is the channel height). For $\Delta T > 0$ and $\mu^* = 0$, the critical Rayleigh number was found to be 1708 which agrees well with Gage and Reid⁶ and the resulting structures were found to be longitudinal rolls.

For stability analyses, the spanwise direction is typically considered to be homogeneous such that a wave ansatz with spanwise wavenumber, β , can be employed. This assumption is valid for radial flows (which are periodic in the circumferential direction) but not for square channel flows which necessarily have a finite aspect ratio. This motivated research concerned with the stability of square channel flows with finite lateral extent. An important finding for RBP flows with finite spanwise extent is that the lateral boundaries (channel side walls) can initiate the longitudinal rolls as seen in various experimental studies. ^{17,18} Luijkx et al¹⁹ investigated the stability of RBP flow in a finite aspect ratio channel for an unstable Rayleigh number. They found that for Reynolds numbers below the critical Reynolds number, transverse rolls that are aligned perpendicular to the flow direction can appear because of the finite span effect. Nevertheless, longitudinal vortex rolls appeared when the Reynolds number was raised above a critical value. A linear stability analysis by Nicolas et al²⁰ revealed that decreasing the lateral extent of the channel has a stabilizing effect on RBP flows. As long as the Rayleigh number is above a critical value, transverse rolls are prevalent for Reynolds numbers below a critical Reynolds number and longitudinal flow structures appear otherwise. Nicolas et al²⁰ also investigated RBP flows with infinite aspect ratio and found that the critical Rayleigh number for 2-D transverse waves increases with Reynolds number which is also in agreement with Gage and Reid. ⁶ Hence, as long as the flow is unbounded in the lateral direction, longitudinal rolls will always develop for $Ra > Ra_c = 1708$ provided $Re < Re_c = 5772$.

According to Gage and Reid,⁶ for $Re < Re_c = 5400$ (or 5772 according to Orszag¹⁴) and $Ra < Ra_c = 1708$, 2-D transverse waves (T-S waves) that are aligned perpendicular to the flow direction are unstable and amplified. Gage and Reid⁶ suggest that the viscous instability of RBP flow may be similar to that of Poiseuille flow except for the nonconstant viscosity for the former. The instability of plane Poiseuille flow has been investigated in considerable detail. Meksyn and Stuart²¹ first predicted that the critical Reynolds number based on maximum velocity and channel half-height is 5000. They also showed that for larger disturbance amplitudes that could likely lead to nonlinear interactions, instability can occur at Reynolds numbers as low as 2900. Thomas²² determined that the critical Reynolds number for plane Poiseuille flow is 5780 and that the critical wavelength is 3.062 times the height of the channel. Orszag¹⁴ solved the Orr-Sommerfeld equation for the

stability analysis of plane Poiseuille flow and found a critical Reynolds number of 5772 in agreement with Thomas. ²² A review paper by Stuart²³ mentions that the Reynolds number for which transition to turbulence occurs in experiments is usually lower than predicted by linear theory. For instance, Kao and Park²⁴ reported a critical Reynolds number (based on hydraulic diameter and bulk velocity) of 2600 (approximately 1097 based on channel half-height and maximum velocity). The experiment was carried out in a channel with an aspect ratio of eight. The low aspect ratio or other factors such as elevated high initial disturbance amplitudes may be responsible for the mismatch between the measured and predicted critical Reynolds number. Nishioka et al²⁵ measured the streamwise development of sinusoidal waves for Reynolds numbers ranging from 3000 to 7500 in a channel with an aspect ratio of 27.4. The spatial disturbance growth was in accordance with LST as long as the initial disturbances were small enough. A nonlinear subcritical (Reynolds number below critical Reynolds number for linear stability) instability was discovered when the disturbance level exceeded a certain threshold value. Chung et al²⁶ carried out direct numerical simulations (DNS) for a subcritical (Re = 5000) and supercritical Reynolds number (Re = 7500) and employed wall-normal blowing and suction for introducing traveling waves. Significant disturbance growth and onset of nonlinearities were observed. A similar investigation of the spatial stability of plane Poiseuille flow for two different Reynolds numbers (2000 and 7500) was carried out by Lee at al.²⁷ They reported a T-S wave phase speed of approximately 0.4 times the centerline velocity.

LST is an effective method for analyzing the primary stability of RBP flows as demonstrated by, for example, Gage and Reid. In this article, temporal stability simulations based on the full and linearized Navier-Stokes equations are proposed as an efficient method for investigating the primary and secondary instability as well as laminar to turbulent transition of RBP flows. Details of two highly accurate temporal codes based on the compressible Navier-Stokes equations that were developed specifically for this purpose are provided. The codes were validated for different 2-D and 3-D cases with buoyancy- and viscosity-driven instability. Although the validation is limited to cases with primary instability, stability analyses of more complicated problems that are difficult or impossible to solve with LST are of course possible. The article concludes with a brief discussion of the results.

2 | METHODOLOGY

2.1 | Governing equations

Temporal stability simulations are proposed as an efficient way to investigate the instability of Rayleigh-Bénard-Poiseuille (RBP) flows. Two numerical approaches were considered: For the first approach, the full nonlinear Navier-Stokes equations are solved. For the second approach, the linearized Navier-Stokes equations are solved. These two approaches are here referred to as DNS and linearized Navier-Stokes simulation (LNS). The governing equations were made dimensionless with a reference velocity, u_{ref} , reference length, L_{ref} , reference temperature, $T_{ref} = 300K$, and reference density, ρ_{ref} . Pressure was non-dimensionalized with $\rho_{ref}u_{max}^2$ and the dynamic viscosity was made dimensionless with μ_{ref} . Unless stated otherwise the maximum velocity, u_{max} , and channel half-height, h/2, were taken as reference velocity and reference length. The reference Mach number was M=0.1.

For the DNS, the compressible Navier-Stokes equations in conservative form are solved,

$$\frac{\partial \mathbf{Q}}{\partial t} + \frac{\partial \mathbf{E}^{(i)}}{\partial x_i} = \mathbf{H},\tag{3}$$

with state vector,

$$\mathbf{Q} = \left[\rho, \rho u, \rho v, \rho w, \rho e\right]^{T},\tag{4}$$

and flux vectors.

$$\mathbf{E}^{(i)} = \begin{bmatrix} \rho u_i \\ \rho u u_i + p \delta_{1i} - \tau_{1i} \\ \rho v u_i + p \delta_{2i} - \tau_{2i} \\ \rho w u_i + p \delta_{3i} - \tau_{3i} \\ u_i (\rho e + p) - u_j \tau_{ij} + q_i \end{bmatrix}.$$
 (5)

The coordinates and velocities corresponding to i=1, 2, 3 are x, y, z and u, v, w in the streamwise, wall-normal, and spanwise direction. The total energy is $e=\epsilon+1/2u_iu_i$, with internal energy, $\epsilon=c_vT$. The source term vector,

$$\mathbf{H} = \begin{bmatrix} 0 \\ \frac{\partial \overline{p}}{\partial x} \\ g(\rho_{ref} - \rho) \\ 0 \\ u\frac{\partial \overline{p}}{\partial x} + vg(\rho_{ref} - \rho) \end{bmatrix}, \tag{6}$$

contains a constant $\partial \overline{p}/\partial x$ term that compensates for the mean streamwise pressure drop resulting from the viscous losses, and a buoyancy term, $g(\rho_{ref}-\rho)$ (Boussinesq approximation), with gravitational acceleration, $g=9.81 \text{m/s}^2$. The assumptions behind the Boussinesq approximation as stated by Spiegel and Veronis²⁸ are satisfied for the present investigations. The shear stress tensor is,

$$\tau_{ij} = \mu \left(\frac{\partial u_i}{\partial x_j} + \frac{\partial u_j}{\partial x_i} - \frac{2}{3} \frac{\partial u_k}{\partial x_k} \delta_{ij} \right) , \tag{7}$$

and the heat flux vector is, $q_i = -k\partial T/\partial x_i$, with thermal conductivity, $k = \mu c_p/Pr$. The Prandtl number is defined as $Pr = \nu/\alpha^*$, where $\nu = \mu/\rho$. The set of equations is closed by the ideal gas equation, $p = \rho RT$, with Sutherland's equation for the dynamic viscosity.

A disturbance ansatz is made for obtaining the linearized Navier-Stokes equations. All flow quantities are split up into a basic flow and disturbance component, for example,

$$u_i = \bar{u}_i + u_i' \ . \tag{8}$$

The linearized compressible Navier-Stokes equations in conservative form can also be written in vector form,

$$\frac{\partial \mathbf{Q}'}{\partial t} + \frac{\partial \mathbf{E}'^{(i)}}{\partial x_i} = \mathbf{H}',\tag{9}$$

with disturbance state vector,

$$\mathbf{Q}' = \begin{bmatrix} \rho' \\ \overline{\rho}u' + \rho'\overline{u} \\ \overline{\rho}v' + \rho'\overline{v} \\ \overline{\rho}w' + \rho'\overline{w} \\ \overline{\rho}e' + \rho'\overline{e} \end{bmatrix}, \tag{10}$$

and flux vectors,

$$\mathbf{E}' = \begin{bmatrix} \overline{\rho}u_i' + \rho'\bar{u}_i \\ \overline{\rho}u'\bar{u}_i + \overline{\rho}\bar{u}u_i' + \rho'\bar{u}\bar{u}_i + p'\delta_{1i} - \tau_{1i}' \\ \overline{\rho}v'\bar{u}_i + \overline{\rho}vu_i' + \rho'\bar{v}\bar{u}_i + p'\delta_{2i} - \tau_{2i}' \\ \overline{\rho}w'\bar{u}_i + \overline{\rho}wu_i' + \rho'\overline{w}\bar{u}_i + p'\delta_{3i} - \tau_{3i}' \\ (\overline{\rho}\bar{e})u_i' + \bar{u}_i(\overline{\rho}e' + \rho'\bar{e}) + (\overline{p}u_i' + p'\bar{u}_i) - (\bar{u}_j\tau_{ij}' + u_j'\bar{\tau}_{ij}) + q_i' \end{bmatrix}.$$

$$(11)$$

The disturbance total energy is $e' = \epsilon' + \bar{u}_i u_i'$, where $\epsilon' = c_v T'$. The source term vector is

$$\mathbf{H}' = \begin{bmatrix} 0 \\ 0 \\ -g\rho' \\ 0 \\ u'\frac{\partial \overline{\rho}}{\partial x} + v'g(1 - \overline{\rho}) - \overline{v}g\rho' \end{bmatrix}. \tag{12}$$

The shear stress tensor is,

$$\tau'_{ij} = \overline{\mu} \left(\frac{\partial u'_i}{\partial x_j} + \frac{\partial u'_j}{\partial x_i} - \frac{2}{3} \frac{\partial u'_r}{\partial x_r} \delta_{ij} \right) + \mu' \left(\frac{\partial \bar{u}_i}{\partial x_j} + \frac{\partial \bar{u}_j}{\partial x_i} - \frac{2}{3} \frac{\partial \bar{u}_r}{\partial x_r} \delta_{ij} \right)$$
(13)

and the heat flux vector is,

$$q_i' = -\left(\overline{k}\frac{\partial T'}{\partial x_i} + k'\frac{\partial \overline{T}}{\partial x_i}\right). \tag{14}$$

The disturbance component of the dynamic viscosity and heat conductivity are

$$\mu' = \frac{\partial \overline{\mu}}{\partial \overline{T}} T' \tag{15}$$

and

$$k' = \frac{\partial \overline{k}}{\partial \overline{T}} T' = \frac{c_p}{Pr} \frac{\partial \overline{\mu}}{\partial \overline{T}} T'. \tag{16}$$

The disturbance pressure is

$$p' = R(\rho'\overline{T} + \overline{\rho}T'). \tag{17}$$

2.2 | Wall-normal grid point distribution and discretization

A coordinate transformation is employed in the wall-normal direction (grid line index, j; coordinate in computational space, $\eta = j$; $\Delta \eta = 1$) that clusters grid points near the walls. A total of J grid points are distributed in the wall-normal direction,

$$y_j = \left[\frac{\tan^{-1}(jc^* - f_1)}{f_2} + 1 \right] \frac{h}{2},\tag{18}$$

where h is the channel height, $c^* = 0.05$ is a user-specified constant, $f_1 = Jc^*/2$, and $f_2 = \tan^{-1}(f_1)$. The derivative of the computational coordinate with respect to the physical coordinate is,

$$\frac{\partial \eta}{\partial y} = 2 \frac{f_2}{c^* h} \left\{ 1 + \tan^2 \left[\left(\frac{2y}{h} - 1 \right) f_2 \right] \right\},\tag{19}$$

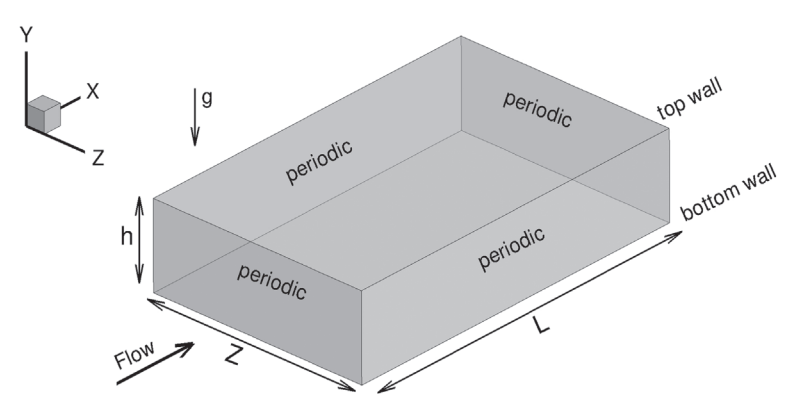
and derivatives in physical space can be obtained from

$$\frac{\partial f}{\partial v} = f' \frac{\partial \eta}{\partial v}.$$
 (20)

A schematic of the computational domain that illustrates the coordinate system, geometric dimensions, temperature boundary conditions, and direction of the flow and gravitational acceleration is provided in Figure 1.



FIGURE 1 Schematic of computational domain



The first derivatives of the convective terms are discretized with fifth-order-accurate upwind-biased,

$$\frac{1}{2}f'_{j-1} + f'_{j} + \frac{1}{6}f'_{j+1} = -\frac{1}{18}f_{j-2} - f_{j-1} + \frac{1}{2}f_{j} + \frac{5}{9}f_{j+1},\tag{21}$$

and downwind-biased,

$$\frac{1}{2}f'_{j+1} + f'_j + \frac{1}{6}f'_{j-1} = \frac{1}{18}f_{j+2} + f_{j+1} - \frac{1}{2}f_j - \frac{5}{9}f_{j-1},\tag{22}$$

compact finite differences.²⁹ For the spatial discretization of the first and second derivatives that appear in the viscous terms, fourth-order-accurate compact finite differences for nonequidistant meshes by Shukla et al,³⁰

$$a_{j-1}f_{j-1}^{(d)} + f_j^{(d)} + a_{j+1}f_{j+1}^{(d)} = b_{j-1}f_{j-1} + b_jf_j + b_{j+1}f_{j+1},$$
(23)

are utilized. Here d (either 1 or 2) represents the order of the derivative. The coefficients a_{j-1} , a_{j+1} , b_{j-1} , b_j and b_{j+1} can be found in Shukla et al.³⁰ The resulting tridiagonal systems of equations are solved with the Thomas algorithm. Streamwise and spanwise derivatives are calculated in Fourier space. It has to be noted that simulations can only be referred to as DNS as long as all scales of fluid motion are captured with minimal amplitude and phase error. The use of Fourier modes for the present simulations guarantees spectral resolution in the streamwise and spanwise directions and thus satisfies this criterion. The forward and backward Fourier transforms are computed with fast Fourier transforms. A fourth-order-accurate Runge-Kutta method³¹ is employed for advancing the governing equations in time. Both the DNS and LNS code have been implemented in Fortran.

2.3 | Boundary conditions

For the DNS, no-slip and no-penetration boundary conditions are enforced at the walls. The bottom (T_b) and top wall (T_t) temperature are held constant. Assuming $\partial \rho v/\partial t = 0$ and $\partial/\partial x = 0$ at the wall, the momentum equation in the *y*-direction at the wall simplifies to

$$\frac{\partial p}{\partial y} = g(1 - \rho). \tag{24}$$

The pressure differential is discretized with a one-sided fourth-order-accurate standard finite difference stencil, leading to the following expression for the wall pressure at the bottom and top wall,

$$p_0 = \frac{-12g\frac{\partial y}{\partial \eta} + 48p_1 - 36p_2 + 16p_3 - 3p_4}{25 - \frac{12g}{RT_0}\frac{\partial y}{\partial \eta}},$$
(25)

-WILFY-7

and

$$p_J = \frac{12g\frac{\partial y}{\partial \eta} + 48p_{J-1} - 36p_{J-2} + 16p_{J-3} - 3p_{J-4}}{25 + \frac{12g}{RT_J}\frac{\partial y}{\partial \eta}}.$$
 (26)

For the LNS, the streamwise, wall-normal and spanwise disturbance velocity, u', v' and w', as well as the disturbance temperature, T', are set to zero at both the top and bottom wall. The linearized wall-normal momentum equation at the wall simplifies to $\partial p'/\partial y = -g\rho'$. By making use of T'=0 in Eq. 17, an expression for the disturbance density at the wall is obtained, $\rho'=p'/R\overline{T}$. Using one-sided fourth-order-accurate standard finite difference stencils, the disturbance wall pressure at the bottom and top wall can be found,

$$p_0' = \frac{48p_1' - 36p_2' + 16p_3' - 3p_4'}{25 - \frac{12g}{R\overline{T}_0} \frac{\partial y}{\partial \eta}},$$
(27)

and

$$p_{J}' = \frac{48p_{J-1}' - 36p_{J-2}' + 16p_{J-3}' - 3p_{J-4}}{25 + \frac{12g}{R\overline{T}_{J}} \frac{\partial y}{\partial \eta}}.$$
 (28)

2.4 | Basic flow

The basic flow for the DNS and LNS simulations was obtained by solving the one-dimensional (1-D) Navier-Stokes equations with a second-order-accurate shooting method. The equations governing 1-D laminar plane RBP flow are,

$$\frac{\partial p}{\partial x} = \mu \frac{\partial^2 u}{\partial v^2},\tag{29}$$

$$\frac{\partial p}{\partial y} = (1 - \rho)g,\tag{30}$$

$$k\frac{\partial^2 T}{\partial y^2} + \mu \left(\frac{\partial u}{\partial y}\right)^2 = 0. \tag{31}$$

The equations were derived from the incompressible Navier-Stokes equations assuming steady parallel flow. Figure 2 shows the streamwise velocity, temperature and pressure profiles for $T_t = 300K$ and two different wall-normal temperature gradients ($T_b - T_t = 50K$ and 200K).

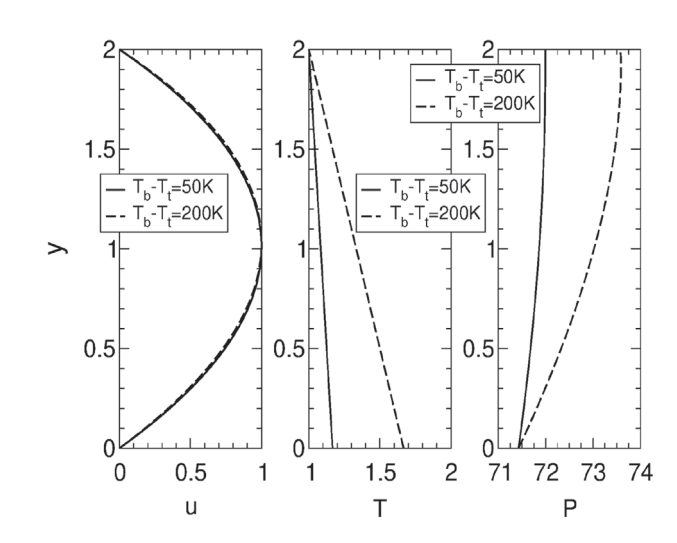


FIGURE 2 Basic flow profiles for two different wall-normal temperature gradients: $T_b - T_t = 50K$ and 200K

2.5 | Numerical linear stability analysis

Very small (linear) random disturbances were added to all five state vector elements before the start of the simulations to raise the initial disturbance amplitudes slightly above machine roundoff and the temporal growth and decay of the resulting waves was investigated. For both DNS and LNS, the random disturbances were added globally (for every grid point) to excite all spanwise (for the buoyancy-driven instability), streamwise (for the viscosity-driven instability) and streamwise and spanwise modes (for the oblique wave investigations). According to what is customary in temporal LST, a wave ansatz of the form

$$u_i'(x, y, z, t) = \sum \hat{u}_i(y)e^{i(\alpha x + \beta z - \omega t)}, \tag{32}$$

is made for the disturbances where α , β and $\omega = \omega_r + i\omega_i$ are the streamwise and spanwise wavenumbers as well as the angular frequency. Here, $\hat{u}_i(y)$ are the mode amplitude distributions (corresponding to eigenfunctions for LST). The sum is taken over all streamwise and spanwise Fourier modes. The streamwise, λ_x , and spanwise, λ_z , wavelengths can be obtained from the streamwise and spanwise wavenumbers, $\lambda_x = 2\pi/\alpha$ and $\lambda_z = 2\pi/\beta$. The wavelengths λ_x and λ_z are related to the streamwise, L, and spanwise domain extent, L, via L and L and L and L in this article, Fourier modes are referred to by their streamwise, L, and spanwise, L, and spanwise, L, and spanwise, L and spanwise, L and spanwise, L and spanwise in the wave propagation direction are L and the angular frequency via L and L and the wave angle is L and L and wavenumber in the wave propagation direction are L and L are the streamwise and spanwise wavenumber as the streamwise, L and L

$$u'_{i}(x, y, z, t) = \hat{a}_{cc} \cos \alpha x \cos \beta z + \hat{a}_{cs} \cos \alpha x \sin \beta z + \hat{a}_{sc} \sin \alpha x \cos \beta z + \hat{a}_{ss} \sin \alpha x \sin \beta z. \tag{33}$$

The first subscript of the Fourier coefficients refers to the streamwise direction (cosine and sine mode). The second subscript refers to the spanwise direction. From this, the amplitude and phase of the right (in positive z-direction, "+" superscript) and left-traveling waves (in negative z-direction, "-" superscript),

$$A^{\pm} = \sqrt{(\hat{a}_c^{\pm})^2 + (\hat{a}_s^{\pm})^2},\tag{34}$$

and

$$\psi^{\pm} = \tan^{-1}\frac{\hat{a}_c^{\pm}}{\hat{a}_c^{\pm}},\tag{35}$$

can be obtained, where $\hat{a}_c^+ = (\hat{a}_{cc} - \hat{a}_{ss})/2$, $\hat{a}_s^+ = (\hat{a}_{sc} + \hat{a}_{cs})/2$, $\hat{a}_c^- = (\hat{a}_{cc} + \hat{a}_{ss})/2$ and $\hat{a}_s^- = (\hat{a}_{sc} - \hat{a}_{cs})/2$. The temporal growth rates of the modes are related to the amplitudes via

$$\omega_i = \frac{\partial \ln A}{\partial t}.\tag{36}$$

Because of $\psi = \alpha x + \beta z - \omega_r t$, the phase speed in the x-direction is

$$c_{x} = -\frac{\frac{\partial \psi}{\partial t}}{\frac{\partial \psi}{\partial x}} = \frac{\omega_{r}}{\alpha} \tag{37}$$

and the phase speed in the wave propagation direction is

$$c = \frac{\omega_r}{k_\lambda}. (38)$$

The disturbance amplitudes and growth rates were computed from the disturbance kinetic energy integrated over the channel height. The phase, frequency and phase speed were calculated from the streamwise, wall-normal and spanwise velocity components in the center of the channel.

TABLE 1 Parameters for 2-D and 3-D simulations.

| Cases | Dimensions | Re | Ra | Pr | T_b | \mathbf{T}_t | Type of instability |
|-------------------------------|------------|--------|--------|------|---------|----------------|--------------------------------------|
| Pabiou et al ³² | 3-D | 130.5 | 6300 | 0.72 | 313.15K | 293.15K | Buoyancy-driven (primary) |
| Case 1 | 3-D | 45 | 10 000 | 1 | 350K | 300K | Buoyancy-driven (primary) |
| Case 2 | 3-D | 45 | 6400 | 1 | 350K | 300K | Buoyancy-driven (primary) |
| Case 3 | 3-D | 45 | 10 000 | 1 | 350K | 300K | Buoyancy-driven (Oblique-primary) |
| Orszag ¹⁴ | 2-D | 10 000 | 0 | 0.72 | 300K | 300K | Viscosity-driven (primary) |
| Case 4 | 2-D | 30 000 | 100 | 1 | 350K | 300K | Viscosity-driven (primary) |
| Case 5 | 2-D | 20 000 | 100 | 1 | 350K | 300K | Viscosity-driven (primary) |

3 | RESULTS

The newly developed DNS and LNS codes were validated for several unstable cases in the vicinity of the stability boundaries provided by Gage and Reid⁶ (Table 1). According to Gage and Reid,⁶ for $Re > Re_c = 5400$ (or 5772 according to Orszag¹⁴) and $Ra > Ra_c = 1708$, 3-D waves with a wave angle of 90° are most amplified. For $Re > Re_c$ and $Ra < Ra_c$ viscosity-driven instability leads to the formation of 2-D T-S waves with a wave angle of zero degree.

The parameters for the various simulations are listed in Table 1. The computational timestep was $\Delta t = 0.001$ for the case with buoyancy-driven instability and $\Delta t = 0.00035$ for the case with viscosity-driven instability. For case 1, the computational timestep was halved and exactly the same result was obtained. This can be explained by the fact that the timestep which is limited by the stability boundary of the explicit time integration scheme, is small enough to provide good temporal resolution.

3.1 | Buoyancy-driven instability

3.1.1 Grid resolution study and comparison with experiment

Stability simulations were first carried out for the experimental conditions by Pabiou et al.³² The Prandtl number was Pr = 0.71, and the top and bottom wall temperature were $T_b = 313.15K$ and $T_t = 293.15K$. For a channel with aspect ratio of 10.38, Pabiou et al³² observed 12 longitudinal rolls for $Re_{b1} = 174$ (based on bulk velocity and channel height) and Ra = 6300. The equivalent Reynolds number based on channel maximum velocity and half-height is Re = 130.5. The corresponding spanwise wavenumber is $\beta = 3.63$ ($\lambda_z = 1.73$).

A grid resolution study was carried out using only two spanwise Fourier modes, (0,0) and (0,1). The spanwise grid extent was held constant at $Z = 2 \times \lambda_z = 3.46$. The temporal growth rate was found to converge as the number of grid points, in the wall-normal direction J, was increased (Table 2). Based on this grid convergence study, it was decided to use 72 grid points in the wall-normal direction for the following simulations with buoyancy-driven instability.

A wavelength study was then conducted for Re = 130.5 and Ra = 6300. The DNS results in Figure 3 illustrate that the maximum growth rate is obtained for a spanwise wavelength of $\lambda_z = 3.22$ which corresponds to a spanwise wavenumber of $\beta = 1.9512$ based on channel half-height. This spanwise wavenumber agrees within 7.5% with the spanwise wavenumber observed by Pabiou et al³² in their finite aspect ratio channel flow experiment. In the experiment, the longitudinal rolls were found to be wider near the side walls than in the middle of the channel which may explain the present slight wavenumber mismatch between simulation and experiment.

| J | ω_i |
|-----|------------|
| 48 | 0.086984 |
| 72 | 0.086982 |
| 96 | 0.086981 |
| 120 | 0.086980 |

TABLE 2 Dependence of temporal growth rate on wall-normal number of grid points for Re = 130.5 and Ra = 6300.

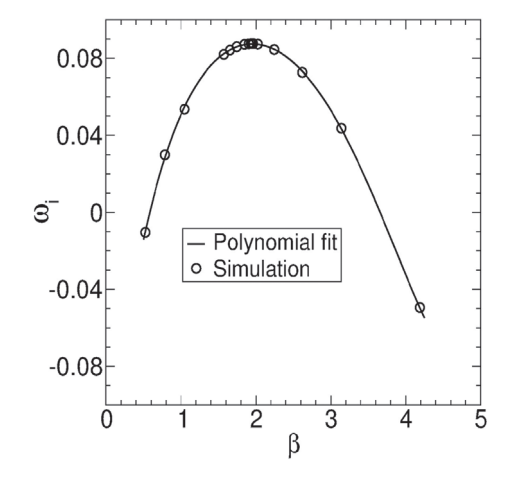
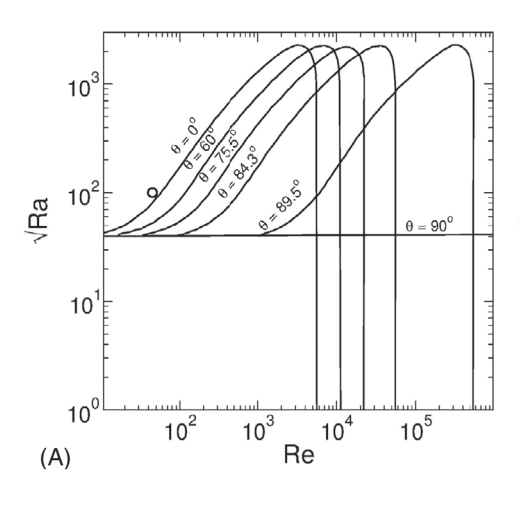


FIGURE 3 Wavelength study: temporal growth rate versus spanwise wavenumber for Re = 130.5 and Ra = 6300



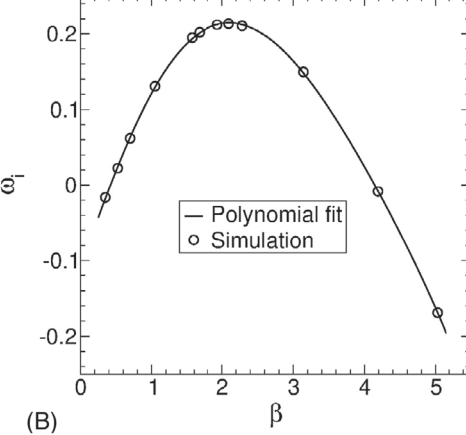


FIGURE 4 A, Stability diagram by Gage and Reid.⁶ symbol (circle) represents conditions for case 1. B, Wavelength study: temporal growth rate versus spanwise wavenumber for case 1

3.1.2 | Case 1: Amplified three-dimensional waves

The Reynolds number and Rayleigh number for case 1 are Re = 45 and $Ra = 10\,000$ (circle in Figure 4A). The bottom and top wall temperature were set to $T_b = 350K$ and $T_t = 300K$. In accordance with Gage and Reid,⁶ the Prandtl number was set to unity. Because the data point for case 1 is above all the neutral curves in Figure 4A, case 1 is expected to be unstable for all wave angles. To determine how the growth rate of the unstable mode depends on the spanwise wavenumber, the spanwise domain extent, Z, was varied (Figure 4B). The highest growth rate ($\omega_i = 0.21349$) is obtained for a spanwise wavenumber of $\beta = 2.0943$ which corresponds to a spanwise wavelength of $\lambda_z = 2\pi/\beta = 3$. The growth rate becomes zero for $\beta \approx 0.42$ and $\beta \approx 4.14$. The very low and very high wavenumbers would of course be difficult to observe in an experiment if all disturbance waves were growing from a uniform background noise level since the $\beta = 2.094$ disturbances grow much faster and develop first into observable flow structures.

After having determined the most unstable spanwise wavelength, a LNS simulation for case 1 with eight spanwise Fourier modes was carried out for a spanwise domain extent of Z = 6 (twice the most unstable wavelength). The mode amplitudes are plotted in Figure 5A. Mode (0,2) corresponding to $\lambda_z = Z/2 = 3$ and $\beta = 2\pi/\lambda_z = 2.0943$ exhibits the strongest linear growth. Modes (0,1) and (0,3) are within the unstable β range according to Figure 4B and grow as a result

FIGURE 5 Mode amplitudes versus time for case 1: A, LNS and, B, DNS

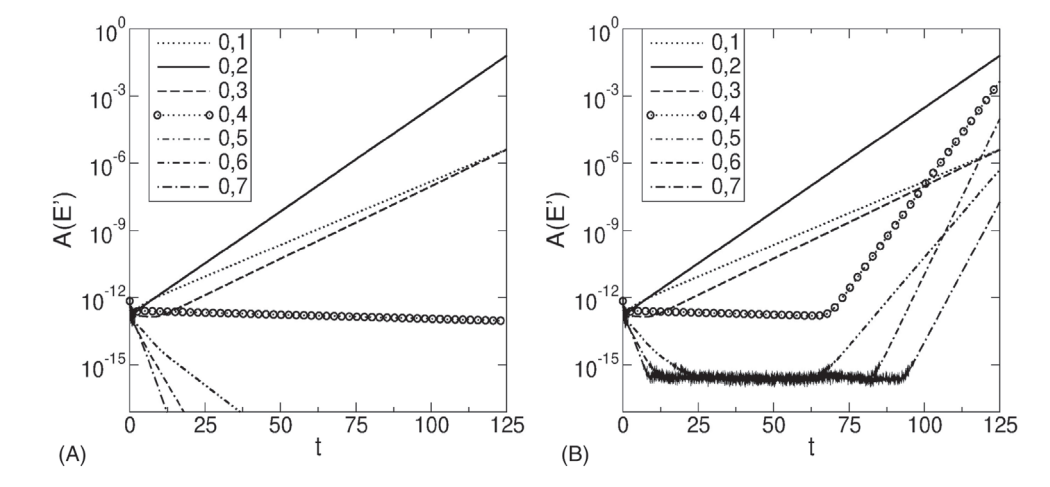
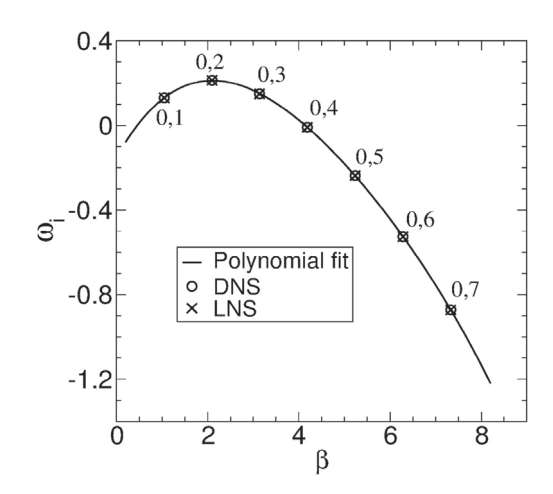


FIGURE 6 Growth rates versus spanwise wavenumber for case 1



of primary instability. Mode (0,4) is close to the stability boundary and weakly damped. The other modes are strongly damped. This is a good example for the utility of the linearized code. The stability of several modes can be investigated with one simulation since the modes are not interacting with each other. The same case (case 1) was also simulated with the DNS code in order to validate the results obtained from the LNS and determine the onset of nonlinearities. The results obtained from the DNS for modes (0,1)-(0,3) are in excellent agreement with the LNS as seen in Figure 5B. In accordance with the LNS, mode (0,2) displays the strongest linear growth. The growth rates obtained from the DNS for t<65 (linear growth or decay) are in excellent quantitative agreement with the LNS as seen in Figure 6. For both approaches, mode (0,2) has the highest growth rate, $\omega_i = 0.21349$. For a domain of span, Z = 6, mode (0,2) has the appearance of two pairs of counter-rotating vortices that are aligned in the streamwise direction. Each vortex pair has a spanwise wavelength of $\lambda_z = 3$.

In the DNS, the waves can interact and departures from linear growth occur for certain modes. All modes initially grow according to the linearized results as seen in Figure 7A. Sudden changes of the growth rates can result from resonance or in general, nonlinear effects. Mode (0,5) is the first to exhibit nonlinear growth. The mode (0,5) nonlinear growth levels off as mode (0,4) begins to grow. The nonlinear growth of mode (0,4) is the strongest for 70 < t < 83 after which it is overshadowed by very strong growth of mode (0,6). Of course, no nonlinear growth is observed in the LNS. The time histories of the phases for the u', v' and w' velocity at the mid-channel height are shown in Figure 7B-D. The phase and growth rate of mode (0,2) obtained from the DNS and LNS are identical which suggests that this mode exhibits primary linear growth. However, for modes that experience nonlinear growth, the phases obtained from the DNS differ considerably from the phases obtained from the LNS. Sudden changes of the growth rates go hand-in-hand with phase adjustments. For example, the suddenly increased growth of mode (0,6) for t > 80 can be associated with a phase alignment of mode (0,6) with mode (0,2) that allows for a nonlinear energy transfer due to resonance. For t > 80 the phase of the

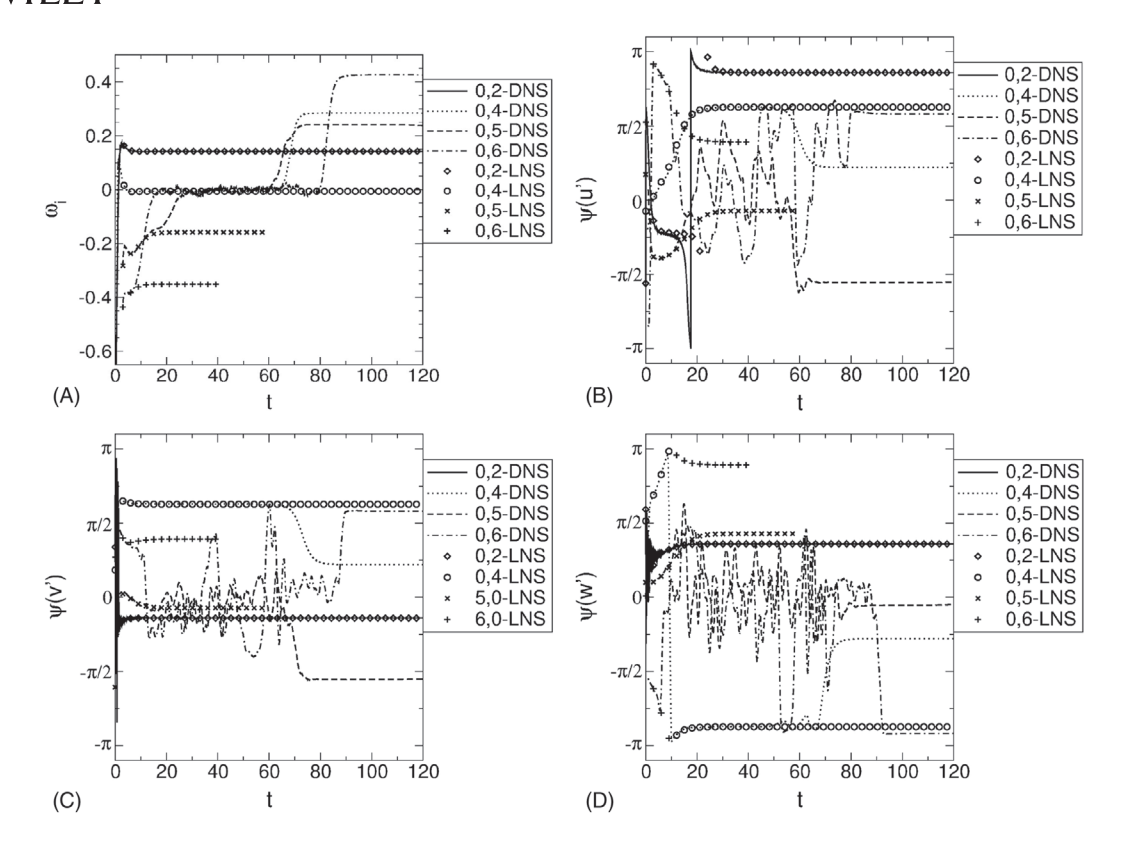


FIGURE 7 Comparison between DNS and LNS results: A, Growth rates vs. time and, B, u', C, v', and, D, w' velocity phase vs. time for case 1

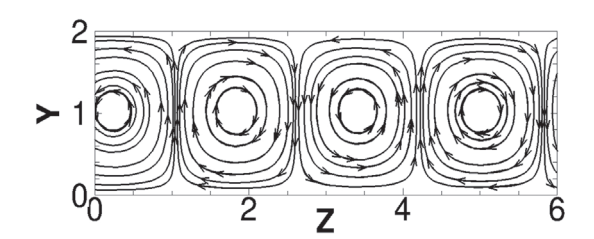


FIGURE 8 Disturbance streamfunction contours at t = 50 for case 1 ($\lambda_z = 3$). Arrows indicate flow direction

wall-normal disturbance velocity is -0.438 for mode (0,2) and 1.825 for mode (0,6). For this phase shift, three wavelengths of mode (0,6) line up with one wavelength of mode (0,2).

Disturbance streamfunction contours obtained from the LNS for t = 50 reveal four counter-rotating cells as seen in Figure 8. The amplitude and phase distributions of the disturbance velocity in the streamwise (u'), wall-normal (v') and spanwise (w') direction for the primary mode (0,2) at t = 100 are provided in Figure 9A,B, respectively. The distributions obtained from the DNS and LNS are identical. The u' and w' amplitude distributions for the primary mode (0,2) have two peaks near $y \approx 1.5$ & $y \approx 0.5$ and a phase-jump of π at $y \approx 1$. The v' disturbance amplitude exhibits only one peak at the mid-channel height and a constant phase distribution.

3.1.3 Case 2: Less strongly amplified three-dimensional waves

For case 2 (Re = 45 and Ra = 6400) the Rayleigh number was lowered compared to case 1 while the Reynolds number and other simulation parameters were kept the same. A comparison of Figures 4B and 10 reveals that lowering the Rayleigh number leads to an increase of the spanwise wavelength of the primary mode to $\lambda_z = 3.25$ and a

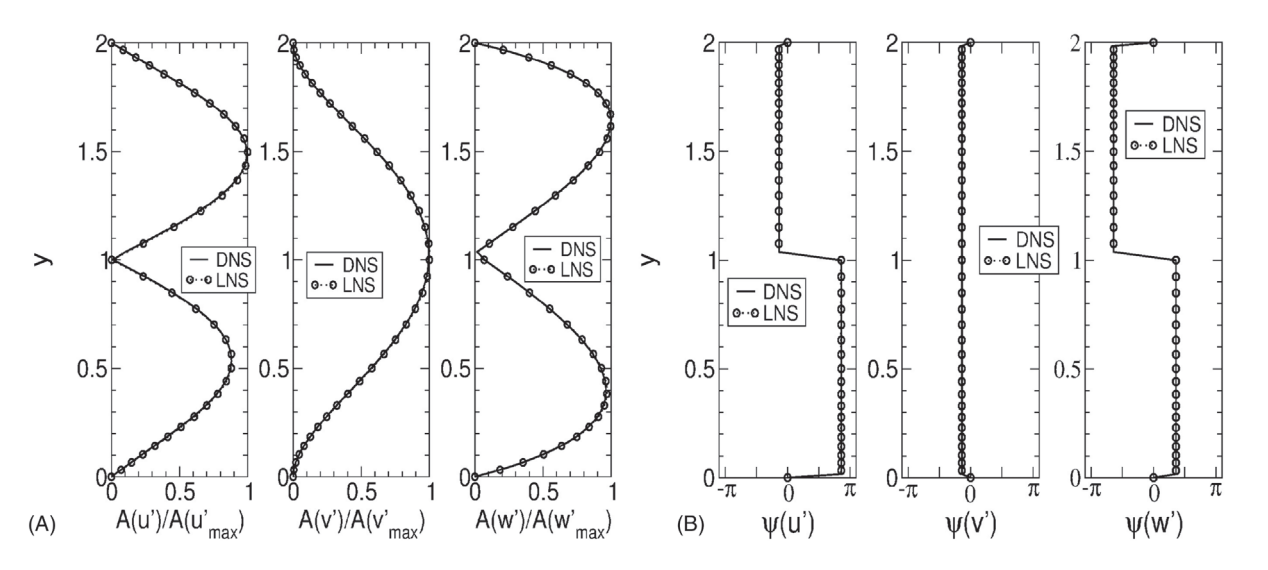
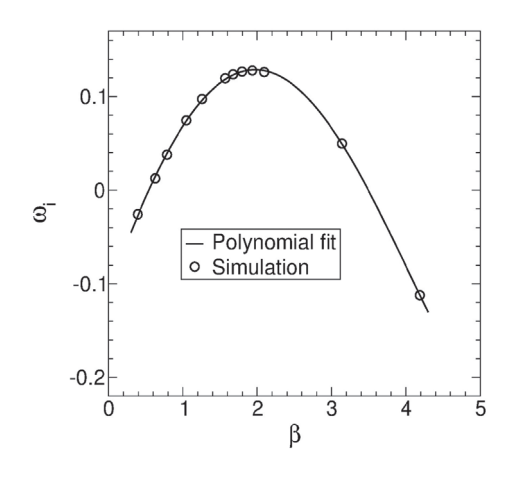


FIGURE 9 Comparison between DNS and LNS: A, mode shapes and, B, phase distributions for mode (0,2) at t = 100 for case 1

FIGURE 10 Growth rate versus spanwise wavenumber for case 2



reduction of the spanwise wavenumber to $\beta = 1.9332$. In addition, the growth rate of the primary mode is reduced to $\omega_i = 0.12794$.

3.1.4 | Case 3: Oblique waves

According to Gage and Reid,⁶ below the critical Reynolds number for the T-S instability, oblique waves can be amplified if the Rayleigh number is large enough. However, transverse waves with a wave angle of $\theta = 90^\circ$ experience the highest amplification (Figure 4A). A series of temporal stability simulations with fixed wavenumber of $k_\lambda = 2.0943$ were carried out with the DNS code for Re = 45 and $Ra = 10\,000$. Only one Fourier mode was used in the streamwise and spanwise directions. The wave angle θ was varied and the streamwise, L, and spanwise, Z, domain extent were chosen as $\lambda = \lambda_x \cos \theta$ and $\lambda = \lambda_z \sin \theta$. In Figure 11, the mode amplitudes for the left and right-traveling waves are plotted versus time. Apart from some minimal differences for t < 3, the amplitudes of the left and right-traveling waves are very similar. This confirms that the random forcing at t = 0 does not favor one family of waves over the other. The growth rates are provided in Table 3. In accordance with Gage and Reid,⁶ the largest growth rate is obtained for $\theta = 90^\circ$. As the wave angle is increased to 90°, the temporal growth rate approaches $\omega_i = 0.21349$ as seen in Table 3 and Figure 12A. The frequency as well as the phase speed are also tabulated in Table 3 and plotted in Figure 12B. Interestingly, with increasing wave angle, both quantities decrease almost linearly and approach zero for $\theta \to 90^\circ$. The u', v' and w' disturbance velocity amplitudes for the left and right-traveling waves are in close agreement as seen in Figure 13A. Figure 13B shows the phase distributions for the left and right-traveling waves which are identical albeit for a small phase shift.

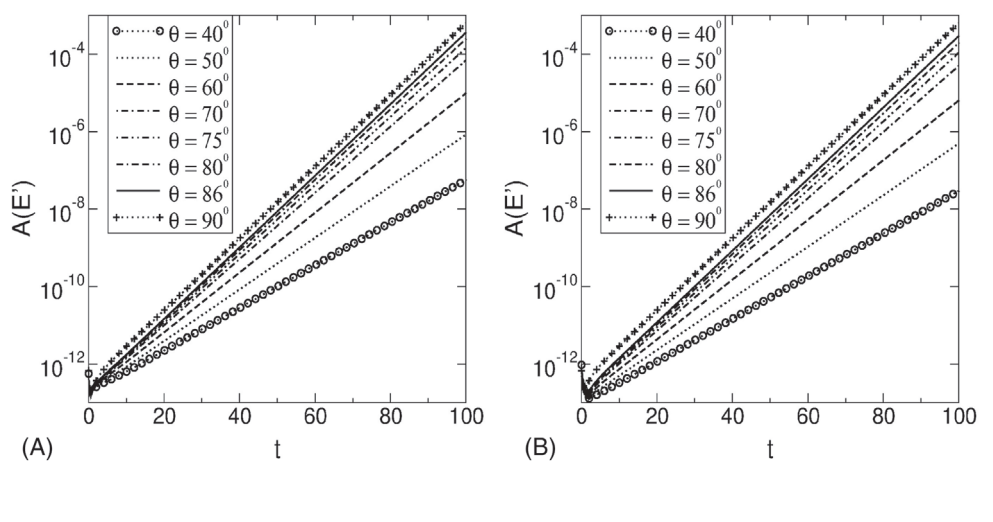
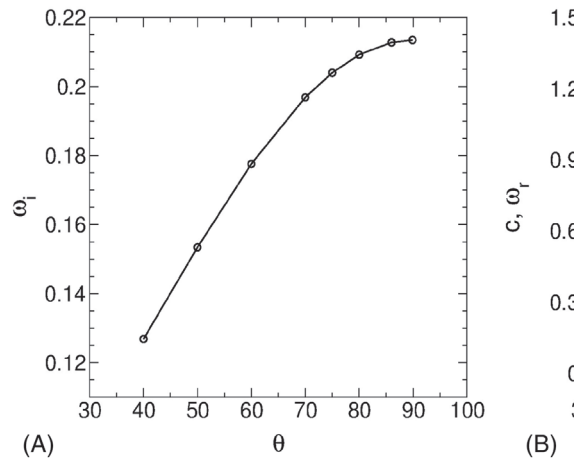


FIGURE 11 Mode amplitudes vs. time for case 3 for, A, left-traveling waves and, B, right-traveling waves



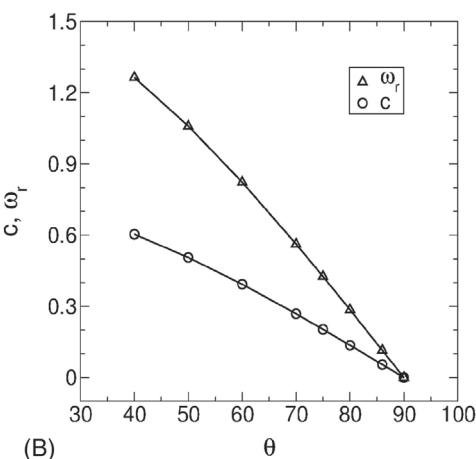


FIGURE 12 A, Growth rate versus wave angle and, B, frequency and phase speed versus wave angle for case 3 (data points are connected by straight lines)

| θ (in deg) | α | β | ω_i | ω_r | c |
|-------------------|--------|--------|------------|------------|--------|
| 40 | 1.6043 | 1.3462 | 0.1268 | 1.2642 | 0.6036 |
| 50 | 1.3462 | 1.6043 | 0.1534 | 1.0593 | 0.5057 |
| 60 | 1.0471 | 1.8137 | 0.1775 | 0.8229 | 0.3929 |
| 70 | 0.7163 | 1.9680 | 0.1968 | 0.5623 | 0.2684 |
| 75 | 0.5420 | 2.023 | 0.2039 | 0.4253 | 0.2030 |
| 80 | 0.3636 | 2.0625 | 0.2092 | 0.2852 | 0.1362 |
| 86 | 0.1460 | 2.0892 | 0.2128 | 0.1145 | 0.0547 |
| 90 | 0 | 2.0943 | 0.2134 | 0 | 0 |

TABLE 3 Growth rate, frequency and phase speed versus wave angle and streamwise and spanwise wavenumber for case 3.

3.2 | Viscosity-driven instability

3.2.1 | Grid resolution study and comparison with literature

Several researchers investigated the onset of hydrodynamic instability in plane Poiseuille flow (no heated walls, no gravitational field) numerically. The first numerical solutions of the Orr-Sommerfeld stability equation were obtained by Thomas²² using a five-point Numerov finite difference method. Using 50 and 100 grid points, Thomas²² found phase speeds of c = 0.2375006 + 0.0035925i and c = 0.2375243 + 0.0037312i, respectively, for $\alpha = 1$ and Re = 10000 (based on channel maximum velocity and half-height). Gary and Helgason³³ employed a sixth-order-accurate finite

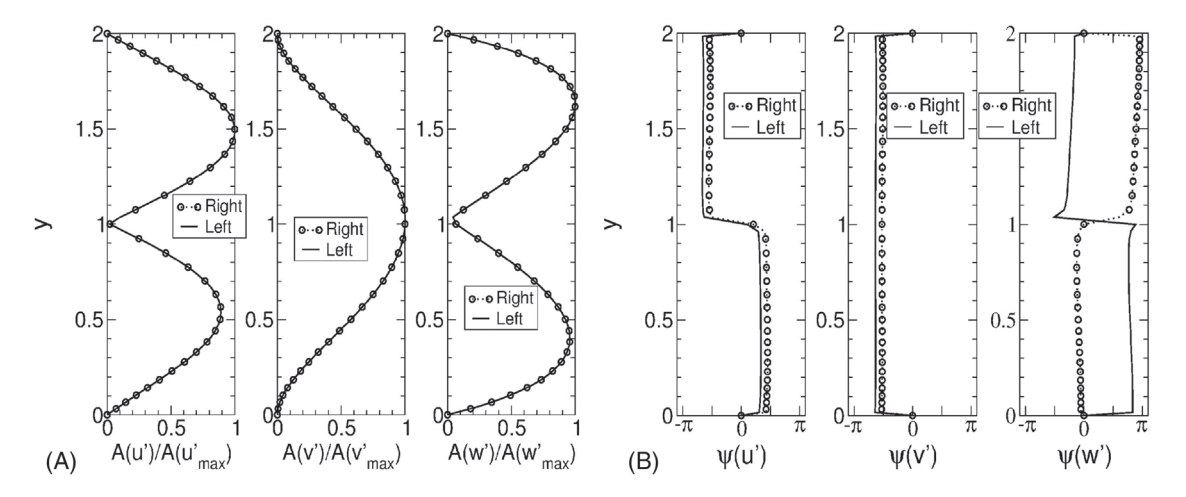


FIGURE 13 A, Mode shapes and, B, phase distributions for $\theta = 80^{\circ}$ at t = 100 for case 3

TABLE 4 Phase speed vs. number of grid points in wall-normal direction and relative error with respect to Orszag.¹⁴

| J | $c = c_r + ic_i$ | $ Error(\%) $ for c_i |
|-----|-------------------|-------------------------|
| 72 | 0.23452+0.005341i | 42.82 |
| 120 | 0.23709+0.003728i | 0.31 |
| 144 | 0.23739+0.003706i | 0.9 |
| 168 | 0.23752+0.003708i | 0.84 |
| 192 | 0.23757+0.003711i | 0.76 |
| 216 | 0.23760+0.003713i | 0.71 |
| 240 | 0.23762+0.003716i | 0.63 |
| 264 | 0.23763+0.003716i | 0.63 |

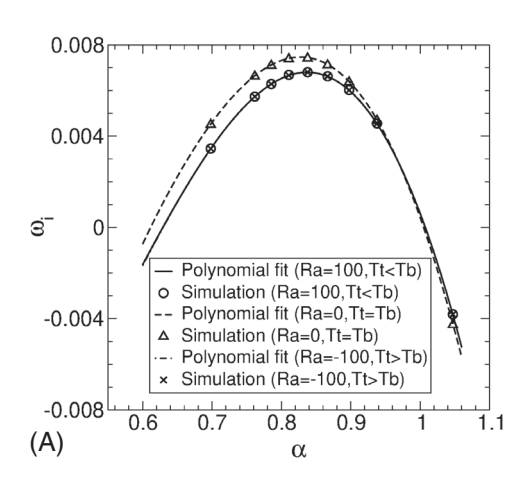
difference scheme for nonequidistant coordinates and obtained c = 0.23752964 + 0.00374248i (43 grid points) and c = 0.23752650 + 0.00373969i (100 grid points) for the same case. An accurate solution of the Orr-Sommerfeld stability equation was achieved by Orszag¹⁴ using Chebyshev polynomials. According to Orszag,¹⁴ the phase speed for $\alpha = 1$ and Re = 10000 is c = 0.23752679 + 0.00373967i. The Orszag¹⁴ case was recomputed to validate the present numerical approach for a case with viscosity-driven instability. The top and bottom wall temperature for this case are $T_b = T_t = 300$ K, and the streamwise domain extent is 2π . Several DNS with different wall-normal grid resolutions were carried out and a phase speed error was calculated with respect to the reference value obtained by Orszag¹⁴ (see Table 4). As the grid resolution is increased, the phase speed obtained from the present simulations converges to a value that is close to the published value in the literature.¹⁴ The small remaining residue error is likely due to the fact that Orszag¹⁴ solved the incompressible Navier-Stokes equations.

3.2.2 | Case 4: Amplified two-dimensional waves

A similar approach as for case 1 was taken to investigate the viscosity-driven instability. The Reynolds number was Re = 30000. According to Gage and Reid,⁶ 2-D disturbances in the form of T-S waves are amplified for $Re > Re_c = 5400$ (or 5772 according to Orszag¹⁴). The Prandtl number was set to one. As for the bouyancy-driven instability, a grid convergence study was carried out first for L = 7 using two streamwise Fourier modes, (0,0) and (1,0). For this grid convergence study, the bottom and top wall temperatures were set to $T_b = 350$ K and $T_t = 300$ K and the Rayleigh number was 100. As the number of wall-normal grid points, J, was increased, the temporal growth rate converged to a value of $\omega_i = 0.006059$ (Table 5). Based on this grid convergence study, the decision was made to use J = 240 grid points for the following simulations with viscosity-driven instability.

 TABLE 5
 Temporal growth rate versus number of grid points in the wall-normal direction for case 4.

| J | ω_i |
|-----|------------|
| 48 | 0.017947 |
| 96 | 0.0081849 |
| 144 | 0.0059285 |
| 192 | 0.0059427 |
| 240 | 0.006059 |
| 288 | 0.006059 |



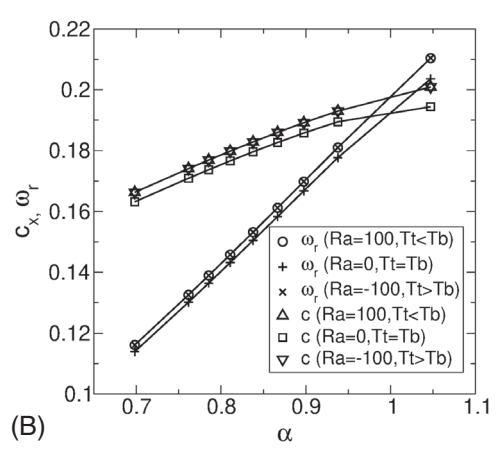


FIGURE 14 Wavelength study: A, growth rates and, B, frequencies and phase speeds versus streamwise wavenumber for $Re = 30\,000$ with Ra = 100 ($T_t < T_b$), Ra = 0 ($T_t = T_b$), and Ra = -100 ($T_t > T_b$)

Although the Rayleigh number is subcritical, the disparate wall temperatures result in a viscosity gradient and thus may have an effect on the viscosity-driven instability. Therefore, two additional cases were considered: For the first additional case, the bottom and top wall temperatures were $T_b = T_t = 300 \text{K}$ and the Rayleigh number was zero. For the second additional case, the bottom and top wall temperatures were set to $T_b = 300 \text{K}$ and $T_t = 350 \text{K}$ and the Rayleigh number was -100. The streamwise domain extent was varied to find the streamwise wavenumber, α , with the highest temporal growth rate. Figure 14 reveals that the growth rates, phase speeds, and frequencies for Ra = 100 ($T_t < T_b$) and Ra = -100 ($T_t > T_b$) are identical. This was expected since the two cases are identical as long as the buoyancy-driven instability is suppressed. Slightly higher growth rates and lower phase speeds and frequencies are obtained when the wall temperatures are identical (Ra = 0). For all cases, disturbances with a streamwise wavelength of $\lambda_x = 7.5$, which corresponds to a wavenumber of $\alpha = 2\pi/\lambda_x = 0.837$, experience the strongest temporal growth. The maximum temporal growth rate is $\omega_i = 0.0068036$ for the cases with differential wall heating and $\omega_i = 0.0074172$ for the case with identical wall heating. The phase speed at the maximum amplification is 0.1828 for |Ra| = 100 (both $T_t < T_b$ and $T_t > T_b$) and 0.1796 for Ra = 0 ($T_t = T_b$). The corresponding frequencies are 0.1531 and 0.15047, respectively. The u' and v' amplitude distributions for $T_t < T_b$ and $T_t > T_b$ are asymmetric with respect to the channel centerline but symmetric with respect to each other (see Figure 15). The amplitude distributions for Ra = 0 are symmetric with respect to the channel centerline.

The streamwise domain extent was then set to two times the wavelength of the most amplified mode ($L = 2 \times 7.5 = 15$). Using eight streamwise Fourier modes, the first case (Ra = 100 with $T_b > T_t$) was analyzed in more detail with both the LNS and DNS code. For both LNS and DNS, in agreement with the earlier wavelength study, the primary mode (2,0) grows linearly as observed in Figure 16. While in the LNS all other modes are decaying, in the DNS modes can grow as a result of nonlinear interactions. The temporal growth rates obtained from the LNS and DNS for the primary wave or fundamental (2,0) are in good agreement. The growth rate is roughly 30 times smaller than the maximum growth rate for the previous case with buoyancy-driven instability (Re = 45 and Ra = 10000). Of course, higher growth rates are expected for larger Reynolds numbers. For t > 1800 strong nonlinear growth of the higher harmonic (4,0) occurs as seen in Figure 16B. Later, mode (6,0) is growing for t > 2500 at an even faster pace. In general, the nonlinear growth rates are larger than the linear growth rates (Figure 17A). Similar observations were made by Nishioka et al²⁵ based on an experimental investigation of plane Poiseuille flow. The onset of nonlinear growth goes hand-in-hand with a matching of the phase speed of the higher harmonic modes with the primary mode as seen in Figure 17B. For example, as the phase speed of mode (4,0) approaches the phase speed of mode (2,0) for t > 1800, energy transfer from mode (2,0) to mode (4,0) becomes possible and mode (4,0)

FIGURE 15 Amplitude of u' and v' disturbance velocity for $Re = 30\,000$ with $Ra = 100\,(T_t < T_b)$, $Ra = 0\,(T_t = T_b)$, and $Ra = -100\,(T_t > T_b)$

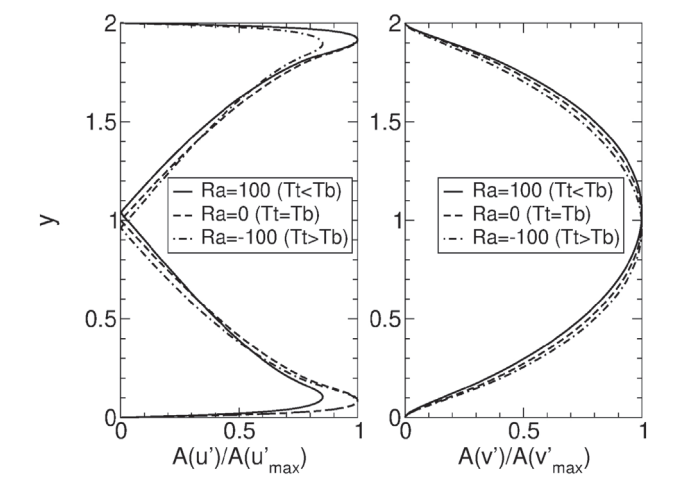


FIGURE 16 Mode amplitudes vs. time for case 4: A, LNS and, B, DNS

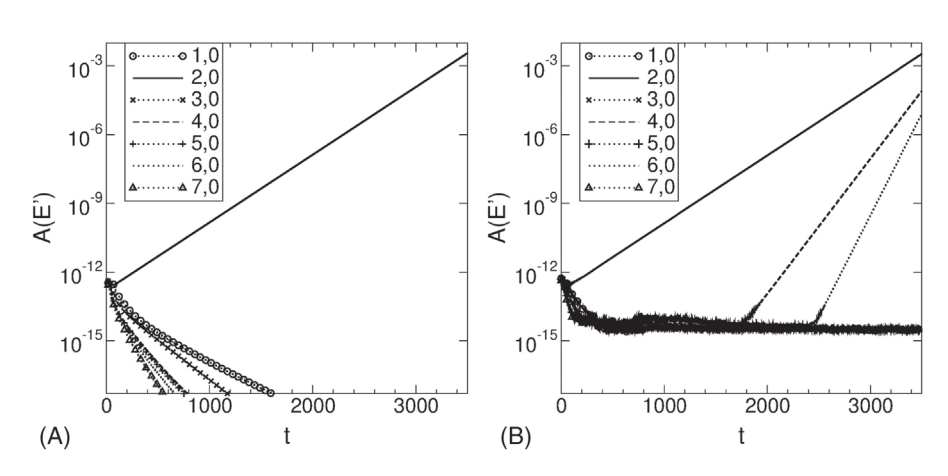
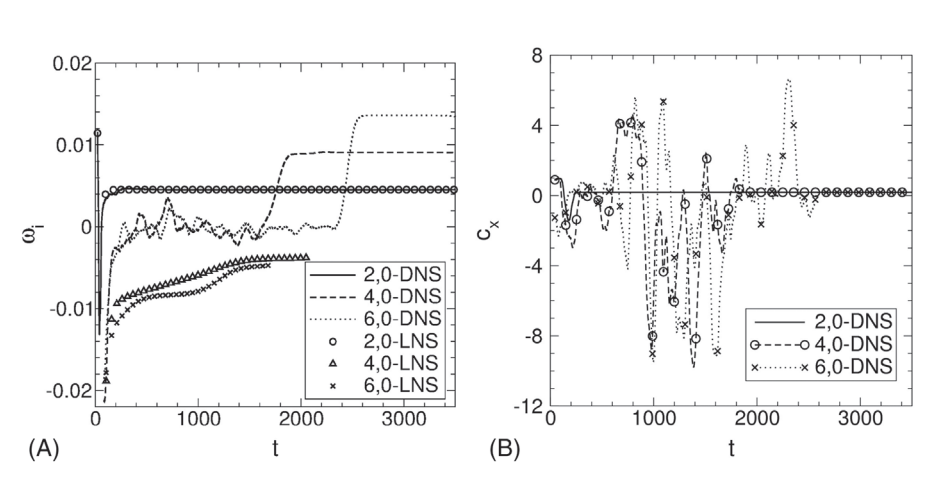


FIGURE 17 A, Growth rates and, B, phase speeds versus time for case 4



begins to grow strongly. Mode (6,0) exhibits a similar behavior. Analogous observations were made in the literature for boundary layer flows.³⁴ For a domain of length of L = 15, mode (2,0) corresponds to two T-S waves with a streamwise wavelength of $\lambda_x = 7.5$.

The u' and v' amplitude and phase distributions for the primary mode (2,0) at t = 3185 are compared in Figure 18. As is typical for T-S waves, the u' mode amplitude has maxima near the top and bottom wall where the viscous effects are stronger. The u' phase distribution has a phase shift of π at $y \approx 1$. On the other hand, the v' amplitude distribution has only one peak at approximately the mid-channel height and the phase remains constant across the channel. Iso-contours of the disturbance streamfunction obtained from the LNS for t = 1400 reveal two T-S waves with a streamwise wavelength of $\lambda_x = 7.5$ (Figure 19).

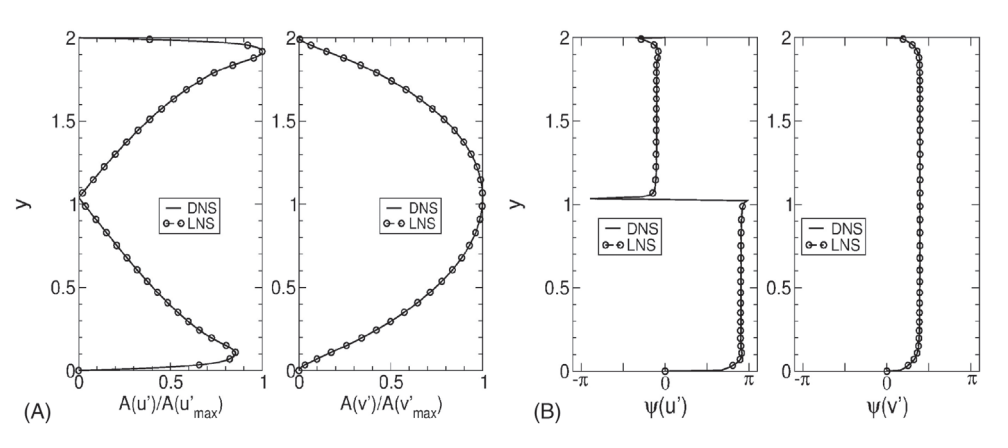


FIGURE 18 A, Amplitude and, B, phase distributions for mode (2,0) at t = 3185 (case 4)

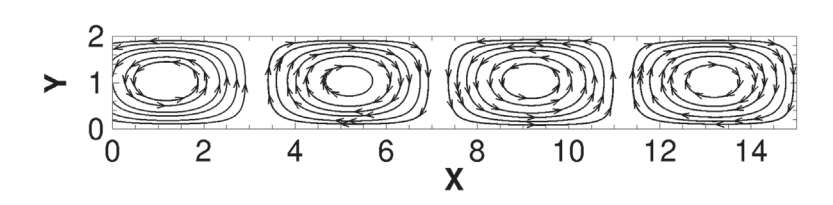


FIGURE 19 Disturbance streamfunction contours at t = 1400 for case 4 ($\lambda_x = 7.5$). Arrows indicate flow direction

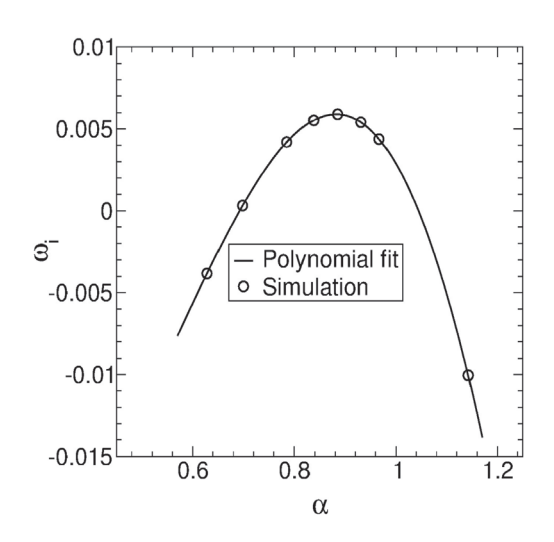


FIGURE 20 Growth rate versus streamwise wavenumber for case 5

3.2.3 Case 5: Less strongly amplified two-dimensional waves

Another DNS simulation was carried out for a lower Reynolds number of 20 000. The Rayleigh number, Ra = 100, Prandtl number, Pr = 1, and bottom and top wall temperatures, $T_b = 350$ K and $T_t = 300$ K, were kept the same as for the previous case. When comparing Figures 14A and 20 it can be seen that both the wavelength and growth rate of the most amplified mode decrease when the Reynolds number is lowered. The streamwise wavelength and temporal growth rate of the most unstable wave are $\lambda_x = 7.1$ ($\alpha = 0.8849$) and $\omega_i = 0.00589$, respectively. The maximum growth rate for Re = 20000 is approximately 13% lower than for Re = 30000.

4 | CONCLUSIONS

A DNS and a LNS code were developed for investigating the stability of Rayleigh-Bénard-Poiseuille (RBP) flows. Stability simulations for a case with buoyancy-driven instability by Pabiou et al³² were in good agreement with the experiment with respect to the spanwise wavelength of the most unstable mode. The buoyancy-driven instability was then investigated for a subcritical Reynolds number and an unstable ($Ra > Ra_c$) Rayleigh number. Using both DNS and LNS, the dependence

of the temporal growth rate of 3-D waves on the spanwise wavenumber, β , was mapped out. For the DNS, the onset of nonlinear effects leads to the strong nonlinear growth of higher harmonics with shorter spanwise wavelength. The spanwise wavelength of the strongest growing higher harmonic has a wavelength of one third the spanwise wavelength of the fundamental. The nonlinear growth is preceded by an adjustment of the spanwise phase of the higher harmonic. Additional simulations revealed that oblique traveling waves were also amplified. As the wave angle increases, the frequency and phase speed of the waves decrease. For a wave angle of 90°, the frequency becomes zero and, in agreement with Gage and Reid,⁶ the growth rate attains its maximum value.

Subcritical Rayleigh numbers were chosen for the investigation of the viscosity-driven instability. As a validation case, the LST results for plane Poiseuille flow by Orszag¹⁴ were recomputed and matched with good accuracy. Two-dimensional DNS and LNS were then carried out for an unstable Reynolds number ($Re > Re_c$). First, the dependence of the temporal growth rate on the streamwise wavelength was determined. For a Reynolds number that is roughly six times higher than the critical Reynolds number, the unstable wavenumber range is quite narrow and the maximum amplification rates are about 30 times lower than for the case with buoyancy-driven instability. As a result, nonlinear effects set in much later. Higher harmonics with a streamwise wavelength that is two and three times shorter compared to the streamwise wavelength of the fundamental are the first to experience nonlinear growth. The onset of the nonlinear effects is initiated by a matching of the phase speeds of the higher harmonics and the fundamental. Assymetric heating of the top and bottom wall lowers the growth rate compared to when the wall temperatures are identical. When the Reynolds number is reduced, the viscosity-driven instability becomes weaker and the streamwise wavelength of the most strongly amplified T-S waves is reduced.

This article serves to introduce two new temporal stability simulation codes that were developed specifically for investigating the stability of RBP flows and to provide validation cases. While much of the published literature on RBP flows considers the spatial case and is often concerned with the finite span effect, the present temporal simulations assume perfect flow periodicity in the spanwise direction and a direct comparison with LST becomes possible. Spanwise periodicity occurs for example for radial RBP flows. For such flows, far enough from the origin, the radial effects can be assumed to be small, and the present temporal analyses provide useful insight into the local stability behavior. For the future, more complex stability investigations are planned that are more difficult or impossible to analyze with LST. Advantageous in the stability analyses context is that DNS and LNS allow for the simultaneous investigation of a large number of modes which saves computer time. For the DNS, as shown in this article, nonlinear interactions are possible that can eventually lead to transition and turbulence.

ACKNOWLEDGMENTS

This material is based upon work supported by the National Science Foundation under grant no. 1510179. The program manager is Dr. Ronald Joslin.

CONFLICT OF INTEREST

The authors declare no potential conflict of interests.

AUTHOR CONTRIBUTIONS

M.K. Hasan and A. Gross carried out the code development. M.K. Hasan did all of the analysis. M.K. Hasan and A. Gross prepared the manuscript.

ORCID

Md Kamrul Hasan https://orcid.org/0000-0003-1328-7234

REFERENCES

- 1. Fasel HF, Meng F, Shams E, Gross A. CFD analysis for solar chimney power plants. *Sol Energy*. 2013;98(Part A):12-22. https://doi.org/10. 1016/j.solener.2013.08.029.
- 2. Hasnaoui M, Bilgen E, Vasseur P, Robillard L. Mixed convective heat transfer in a horizontal channel heated periodically from below. Numer Heat Transf Part A Appl. 1991;20(3):297-315. https://doi.org/10.1080/10407789108944823.
- 3. Zhang SQ, Tangborn AV. Flow regimes in two-dimensional mixed convection with spatially periodic lower wall heating. *Phys Fluids*. 1994;6(10):3285-3293. https://doi.org/10.1063/1.868061.
- 4. Jensen KF, Einset EO, Fotiadis DI. Flow phenomena in chemical vapor deposition of thin films. *Ann Rev Fluid Mech.* 1991;23:197-233. https://doi.org/10.1146/annurev.fl.23.010191.001213.

- 5. Evans G, Greif R. Thermally unstable convection with applications to chemical vapor deposition channel reactorst. *Int J Heat Mass Transf*. 1993;36(11):2769-2781. https://doi.org/10.1016/0017-9310(93)90096-O.
- Gage KS, Reid WH. The stability of thermally stratified plane Poiseuille flow. J Fluid Mech. 1968;33(1):21-32. https://doi.org/10.1017/ S0022112068002326.
- 7. Miles JW. On the stability of heterogeneous shear flows. J Fluid Mech. 1961;10:496-508. https://doi.org/10.1017/S0022112061000305.
- 8. Koppel D. On the stability of flow of a thermally stratified fluid under the action of gravity. *J Math Phys.* 1964;5(7):963-982. https://doi.org/10.1063/1.1704198.
- 9. Busse FH. On the stability of two-dimensional convection in a layer heated from below. *J Math Phys.* 1967;46(1–4):140-150. https://doi.org/10.1002/sapm1967461140.
- 10. Clever RM, Busse FH. Transition to time-dependent convection. *J Fluid Mech.* 1974;65:625-645. https://doi.org/10.1017/S0022112074001571.
- 11. Clever RM, Busse FH. Low-Prandtl-number convection in a layer heated from below. *J Fluid Mech.* 1981;102:61-74. https://doi.org/10. 1017/S002211208100253X.
- 12. Assenheimer M, Steinberg V. Observation of coexisting upflow and downflow hexagons in Boussinesq Rayleigh-Bénard convection. *Phys Rev Lett.* 1996;76(5):756-759. https://doi.org/10.1103/PhysRevLett.76.756.
- Clever RM, Busse FH. Hexagonal convection cells under conditions of vertical symmetry. Phys Rev E. 1996;53(3):R2037-R2040. https://doi.org/10.1103/physreve.53.r2037.
- 14. Orszag SA. Accurate solution of the Orr-Sommerfeld stability equation. *J Fluid Mech.* 1971;50(4):689-703. https://doi.org/10.1017/S0022112071002842.
- 15. Mori Y, Uchida Y. Forced convective heat transfer between horizontal flat plates. *Int J Heat Mass Transf*. 1966;9(8):803-808. https://doi.org/10.1016/0017-9310(66)90007-X.
- 16. Nakayama W, Hwang GJ, Cheng KC. Thermal instability in plane poiseuille flow. *J Heat Transf*. 1970;92(1):61-68. https://doi.org/10.1115/1.3449646.
- 17. Chang MY, Yu CH, Lin TF. Changes of longitudinal vortex roll structure in a mixed convective air flow through a horizontal plane channel: an experimental study. *Int J Heat Mass Transf*. 1997;40(2):347-363. https://doi.org/10.1016/0017-9310(96)00098-1.
- 18. Chang MY, Lin TF. Experimental study of aspect ratio effects on longitudinal vortex flow in mixed convection of air in a horizontal rectangular duct. *Int J Heat Mass Transf*. 1998;41(4–5):719-733. https://doi.org/10.1016/S0017-9310(97)00165-8.
- 19. Luijkx JM, Platten JK, Legros JC. On the existence of thermoconvective rolls, transverse to a superimposed mean Poiseuille flow. *Int J Heat Mass Transf*. 1981;24(7):1287-1291. https://doi.org/10.1063/1.3006057.
- 20. Nicolas X, Luijkx JM, Platten JK. Linear stability of mixed convection flows in horizontal rectangular channels of finite transversal extension heated from below. *Int J Heat Mass Transf*. 2000;43(4):589-610. https://doi.org/10.1016/S0017-9310(99)00099-X.
- 21. Meksyn D, Stuart JT. Stability of viscous motion between parallel planes for finite disturbances. *Proc Royal Soc A*. 1951;208(1095):517-526. https://doi.org/10.1098/rspa.1951.0177.
- 22. Thomas LH. The stability of plane Poiseuille flow. Phys Rev. 1953;91(4):780-783. https://doi.org/10.1103/PhysRev.91.780.
- 23. Stuart JT. Nonlinear stability theory. Ann Rev Fluid Mech. 1971;3(4):347-370. https://doi.org/10.1146/annurev.fl.03.010171.002023.
- 24. Kao TW, Park C. Experimental investigations of the stability of channel flows. Part 1. flow of a single liquid in a rectangular channel. *J Fluid Mech.* 1970;43(1):145-164. https://doi.org/10.1017/S0022112070002288.
- 25. Nishioka M, Iida S, Ichikawa Y. An experimental investigation of the stability of plane Poiseuille flow. *J Fluid Mech.* 1975;72(4):731-751. https://doi.org/10.1017/S0022112075003254.
- 26. Chung YM, Sung HJ, Boiko AV. Spatial simulation of the instability of channel flow with local suction/blowing. *Phys Fluids*. 1997;9(11):3258-3266. https://doi.org/10.1063/1.869423.
- 27. Lee C, Min T, Kim J. Stability of a channel flow subject to wall blowing and suction in the form of a traveling wave. *Phys Fluids*. 2008;20(10) 101513:1-8. https://doi.org/10.1063/1.3006057.
- 28. Spiegel EA, Veronis G. On the Boussinesq approximation for a compressible fluid. *Astrophys J.* 1960;131:442-447. https://doi.org/10.1086/146849.
- 29. Fan P. The standard upwind compact difference schemes for incompressible flow simulations. *J Comput Phys.* 2016;322:74-112. https://doi.org/10.1016/j.jcp.2016.06.030.
- 30. Shukla RK, Tatineni M, Zhong X. Very high-order compact finite difference schemes on non-uniform grids for incompressible Navier-Stokes equations. *J Comput Phys.* 2007;224(2):1064-1094. https://doi.org/10.1016/j.jcp.2006.11.007.
- 31. Fyfe DJ. Economical evaluation of Runge-Kutta formulae. Math Comput. 1966;20(95):392-398. https://doi.org/10.2307/2003593.
- 32. Pabiou H, Mergui S, Bénard C. Wavy secondary instability of longitudinal rolls in Rayleigh-Bénard-Poiseuille flows. *J Fluid Mech.* 2005;542:175-194. https://doi.org/10.1017/S0022112005006154.
- 33. Gary J, Helgason R. A matrix method for ordinary differential eigenvalue problems. *J Comput Phys.* 1970;5(2):169-187. https://doi.org/10. 1016/0021-9991(70)90058-6.
- 34. Herbert T. Secondary instability of boundary layers. *Ann Rev Fluid Mech.* 1988;20:487-526. https://doi.org/10.1146/annurev.fl.20.010188. 002415.

AUTHOR BIOGRAPHIES



Md Kamrul Hasan earned his Bachelor's degree in 2009 from Bangladesh University of Engineering and Technology and his Master of Science degree in 2012 from University of Ulsan, Republic of Korea. Since 2015 he is pursuing a Ph.D. degree in Mechanical Engineering at New Mexico State University.



Andreas Gross earned his doctorate degree in Mechnical Engineering in 2002 from the University of Aachen. From 2005 to 2013 he was a Research Assistant Professor at the University of Arizona. Since 2014 he has served as Assistant and then Associate Professor at New Mexico State University.

SUPPORTING INFORMATION

Additional supporting information may be found online in the Supporting Information section at the end of this article.

How to cite this article: Hasan MK, Gross A. Higher-order-accurate numerical method for temporal stability simulations of Rayleigh-Bénard-Poiseuille flows. *Int J Numer Meth Fluids*. 2020;1–21.

https://doi.org/10.1002/fld.4877